Impact of the tidal p-g instability on the gravitational wave signal from coalescing binary neutron stars

Reed Essick,[1,2] Salvatore Vitale,[1,2] and Nevin N. Weinberg[1]

[1] *Department of Physics and Kavli Institute for Astrophysics and Space Research, Massachusetts Institute of Technology, Cambridge, MA 02139, USA*
[2] *LIGO Laboratory, Massachusetts Institute of Technology, Cambridge, MA 02139, USA*

Recent studies suggest that coalescing neutron stars are subject to a fluid instability involving the nonlinear coupling of the tide to p-modes and g-modes. Its influence on the inspiral dynamics and thus the gravitational wave signal is, however, uncertain because we do not know precisely how the instability saturates. Here we construct a simple, physically motivated model of the saturation that allows us to explore the instability's impact as a function of the model parameters. We find that for plausible assumptions about the saturation, current gravitational wave detectors might miss $> 70\%$ of events if only point particle waveforms are used. Parameters such as the chirp mass, component masses, and luminosity distance might also be significantly biased. On the other hand, we find that relatively simple modifications to the point particle waveform can alleviate these problems and enhance the science that emerges from the detection of binary neutron stars.

arXiv:1609.06362v1 [astro-ph.HE] 20 Sep 2016

I. INTRODUCTION

The detection of gravitational waves (GWs) from binary black holes [2, 3, 37] with the Laser Interferometer Gravitational-wave Observatory [LIGO; 36] opens a new window to our universe and provides the first tests of strong field General Relativity (GR) in vacuum [5]. In the coming years, LIGO also expects to detect GWs from neutron stars (NSs) in coalescing binaries. Although a NS can be treated as a point particle (PP) to a first approximation, at some level tides will modify the rate of inspiral and thus the GW signal. The impact of the tidal effects are, however, uncertain. In part this is due to uncertainties in the NS equation of state, and indeed there is hope that GW observations will eventually provide precise constraints on the equation of state [9, 16, 17, 21, 24, 30]. In addition, there are uncertainties in the tidal fluid dynamics both near the merger when matter and GR effects are strong [19, 31, 46] and during the long inspiral phase when the tide is weakly nonlinear [42–44].

Many previous studies considered the impact of the linear tide, implicitly assuming that nonlinear effects are negligible at GW frequencies below $f \approx 400\,\mathrm{Hz}$. These include studies of the linear equilibrium tide [9, 16, 17, 21, 24, 30] and the linear dynamical tide in non-rotating NSs [22, 25, 32, 35] and rotating NSs [20, 23, 26]. Typically they conclude that linear tidal effects will be difficult to measure with current instruments without a gold-plated detection (signal-to-noise ratios $\gtrsim 50$; [30]) or stacked data from dozens of marginal events [9, 17, 24]. Moreover, because these studies find that tidal effects only become significant during the late inspiral, there are proposals to test vacuum GR using waveforms from NS systems at $f \lesssim 400$ Hz [8].

Recently, it has been suggested that the tide is subject to a weakly nonlinear fluid instability during the early inspiral [42–44, hereafter, WAQB, VZH, and W16, respectively]. The instability involves a non-resonant coupling between the quasi-static equilibrium tide, pressure supported p-modes, and buoyancy (i.e., gravity) supported g-modes. Typically, modes first become unstable at $f \approx 50\,\mathrm{Hz}$ and are driven thereafter to potentially large amplitudes. This continuous transfer of energy from the orbit into the modes increases the rate of inspiral and induces an evergrowing phase shift relative to the PP waveform. Although there has been disagreement in the literature about the magnitude of the growth rates, all studies of p-g coupling predict an instability. Furthermore, W16 find that non-static tidal effects (e.g. compressibility) enhance the growth rates, enabling a very large number of modes to reach significant amplitudes well before the binary merges.

Studies of the p-g instability have mainly focused on calculating the instability threshold and growth rates; they have not attempted to study its saturation in any detail. As a result, we do not know the rate at which the instability extracts energy from the orbit and thus we cannot say precisely how it will impact the GW signal. Because solving for the saturation is challenging and likely subject to uncertainties of its own, here we set a more modest goal. We construct a parametrized model of the saturation and explore the instability's impact as a function of the model parameters. Our saturation model is relatively simple, adding just three new parameters to the 15 already present in the spinning PP model. It is worth emphasizing, however, that although we believe our saturation model adequately captures the range of possibilities, without a proper saturation study we cannot be certain.

The paper is structured as follows. § II reviews the properties of the p-g instability and discusses the physics of its saturation and the uncertainties therein. § III describes our parameterized model of the saturation which we use to explore the tide-induced modifications to the PP waveform. Using Bayesian methods, which we describe in § IV, we then study how the modified waveforms affect source detectability and parameter bias if

the tidal effects are neglected (§ V) and how well we can measure the tidal effects if they are included (§ VI). We summarize and conclude in § VII.

II. NONLINEAR TIDAL INSTABILITY

As the NS inspirals and the amplitude of its tidal deformation increases, the tidal flow becomes susceptible to nonlinear fluid instabilities. These will initially manifest as weakly nonlinear interactions between the tide and internal oscillations modes of the star. WAQB applied the formalism developed in Weinberg et al. [45] to determine the influence of such nonlinear interactions on the inspiral of NS binaries. This revealed a new form of nonlinear instability in which the tide excites a high-frequency p-mode coupled to a low-frequency g-mode. Because the p-mode's (linear eigen-) frequency is much higher than the tidal frequency, the p-g pair is not resonant with the tide. This form of three-wave interaction is therefore very different from the well-known resonant parametric instability in which the tide excites a pair of g-modes whose frequencies approximately sum to the tidal frequency.[1]

In analyzing the growth rates of the p-g instability, WAQB considered only three-wave interactions between the tide, a p-mode, and a g-mode. VZH showed that four-wave interactions between the tide (twice) and two g-modes enter the analysis at the same order as the three-wave interactions. They found that the four-wave interactions significantly cancel the three-wave interactions and concluded that, although the $m = \pm 2$ component of the equilibrium tide can be p-g unstable, the growth rates are too small to influence the inspiral in a measurable way.

However, the analysis in VZH assumes that the equilibrium tide is incompressible. Although that is the case for the static equilibrium tide (the $m = 0$ component), the non-static equilibrium tide ($m \pm 2$) is compressible. W16 accounted for this compressibility and found that it undoes the cancellation between the three- and four-wave interactions, yielding rapid p-g growth rates even during the early inspiral. Specifically, W16 found that the instability turns on at gravitational wave frequencies

$$f_i \simeq 45 \left(\frac{\omega_g}{10^{-4} \lambda \omega_0} \right)^{1/2} \text{Hz}, \tag{1}$$

where ω_g is the g-mode's linear eigenfrequency, $\omega_0 = (GM/R^3)^{1/2}$ is the dynamical frequency of the NS with radius R and mass M, and $\lambda(a) \sim 0.1 - 1$ is a slowly undulating function of binary separation a that depends on how close the equilibrium tide is to a resonance (see Fig. 9 in W16). On resonance, the tide is especially compressible and is more properly referred to as the dynamical tide.

From Equation (1), we see that low frequency g-modes become unstable first. However, it is not clear what sets the minimum ω_g. W16 showed that, for $\omega_g \gtrsim 10^{-4}\omega_0$ (which corresponds to $\ell = 2$ g-modes with radial order $n \lesssim 10^3$), linear damping of the modes does not modify the instability threshold nor the growth rates. However, it is possible that other physical effects will limit the minimum ω_g (e.g., magnetic fields). As we describe in Section III, our saturation model therefore includes a parameter that accounts for the uncertainty in f_i.

Once unstable, the coupled p-modes and g-modes are continuously driven by the tide and their energy grows at a rate

$$\Gamma \approx 2\lambda\epsilon\omega_0 \simeq \frac{20\lambda}{1+q} \left(\frac{f}{100\,\text{Hz}} \right)^2 \text{Hz}, \tag{2}$$

where $\epsilon = (M_2/M_1)(R_1/a)^3$ is the tidal factor, $q = M_1/M_2$ is the ratio of the NS mass to the companion mass, and we assume $\omega_0 = 10^4\,\text{rad}\,\text{s}^{-1}$ (Equation (112) from W16 multiplied by two to yield the growth rate of the energy rather than the amplitude). Note that Γ is independent of ω_g, unlike f_i. Because the modes have enough time to grow by many tens of e-foldings before the binary merges (see W16 Section 5.4), eventually they reach such large energies that their growth saturates due to nonlinear damping (i.e., by exciting secondary waves through nonlinear wave-wave interactions). At saturation, there is a balance between continuous driving by the tide and decay through nonlinear damping. This suggests that the excited modes will continuously dissipate orbital energy at a rate

$$\dot{E}_{NL} \approx \Gamma N E_{\text{sat}}, \tag{3}$$

where N is the number of independently unstable modes. The value of N is uncertain, but since the modes do not need to be resonant, $N \sim 10^3 - 10^4$ is possible based on the modes' typical radial order and angular degree ($n \sim 1000$, $\ell \sim$ few). Given $\dot{E}_{NL}$, we can calculate the cumulative phase shift of the GW signal relative to the PP signal (see Appendix A for details)

$$\Delta\phi(f) \approx 2\pi \int_{f_i}^{f} \frac{\dot{E}_{NL}}{\dot{E}_{\text{gw}}} \tau df, \tag{4}$$

where $\dot{E}_{\text{gw}}$ is the GW luminosity and $\tau = f/\dot{f}$ is the inspiral timescale (both of which are dominated by the leading order quadrupole formula for two point masses).

In general, E_{sat} will be a complicated function of Γ, N, the properties of the unstable modes, the NS structure, and the equation of state. Calculating E_{sat} is therefore challenging and beyond the scope of this paper. Nonetheless, we might expect wave breaking to set an approximate upper bound. A wave breaks when $k_r\xi_r \sim 1$, where ξ_r is the amplitude of the wave's radial displacement and

[1] WAQB showed that although some g-modes are also susceptible to the resonant parametric instability during the inspiral, their growth rates are too small to influence the GW signal.

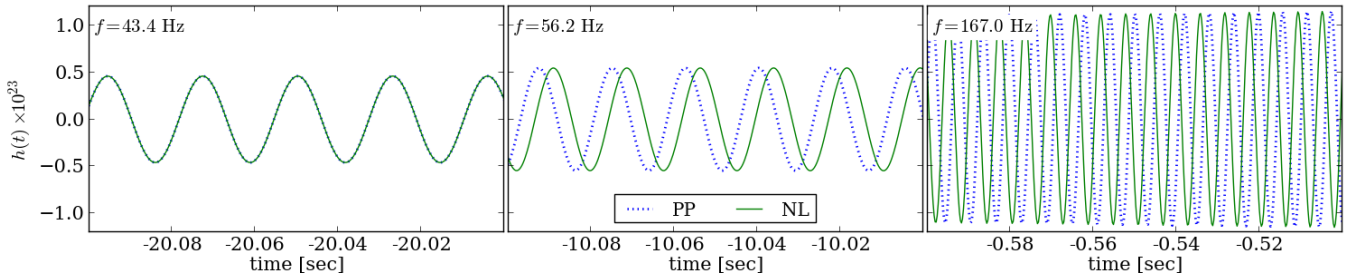

FIG. 1. Time domain GW strain $h(t)$ for a $1.4M_\odot$-$1.4M_\odot$ non-spinning binary NS system at three different stages of the inspiral. The blue dotted curves are the PP waveforms and the green solid curves are the waveforms with nonlinear tidal effects assuming $A = 4 \times 10^{-8}$, $f_0 = 50\,\mathrm{Hz}$, and $n = 0$.

k_r is its radial wavenumber. At wave breaking, a g-mode overturns the local stratification and a p-mode induces order unity density perturbations. WAQB show that g-modes in a NS break at an energy

$$E_{\rm break} \sim 10^{-8} \left(\frac{\omega_g}{10^{-4}\Lambda_g \omega_0}\right)^2 \left(\frac{r}{R}\right)^2 E_0, \qquad (5)$$

where r is the radial location within the star at which the breaking occurs, $\Lambda_g = \ell_g(\ell_g+1)$, and $E_0 = GM^2/R$. This is lower than the energy at which the p-modes break and thus the g-modes probably determine $E_{\rm sat}$ for the p-g instability. Although we use $E_{\rm break} \sim 10^{-8}E_0$ as a reference value throughout our study, note that if the g-modes break at $r \ll R$ the actual value will be much smaller.

These considerations motivate the ansatz $E_{\rm sat} = \beta E_{\rm break}$, where $\beta \to 1$ corresponds to saturation at the g-mode wave breaking energy. Observations of g-mode instabilities in the ocean, the atmosphere, and laboratory experiments often find that saturation indeed occurs by wave breaking (see the review by Staquet & Sommeria [34]). Numerical studies of the dynamical tide in hot Jupiter systems find that g-modes driven by the parametric instability also saturate at energies $E_{\rm sat} \sim E_{\rm break}$ [11, 12, 18]. This suggests that perhaps $\beta \sim 1$ for the p-g instability as well.

To summarize, $\dot{E}_{NL}$ and therefore $\Delta\phi$ are poorly constrained because of uncertainties in the minimum ω_g, the number of unstable modes N, and the saturation energy $E_{\rm sat}$ (or equivalently, β). We now describe how our parameterized model of the saturation accounts for these uncertainties.

III. PARAMETERIZED MODEL OF THE SATURATION

While the saturation of the p-g instability is likely to be a complicated process, we construct a relatively simple model motivated by the theoretical considerations discussed in § II. Given Eqs. (2) and (3), we model the saturation with three parameters (A, f_0, and n) such that

$$\dot{E}_{\rm NL} \propto \lambda f^2 N E_{\rm sat} \propto A f^{n+2} \Theta\left(f - f_0\right), \qquad (6)$$

where Θ is the Heaviside function. The parameters A and n determine the overall magnitude and frequency dependence of $\dot{E}_{\rm NL}$, respectively. The parameter f_0 is the frequency at which the modes reach saturation after becoming unstable. By allowing them to vary, we can account for the uncertainties in f_i, λ, N, and $E_{\rm sat}$ discussed in § II. Our model ignores any dissipation that might occur when $f_i < f < f_0$ and instead assumes that $\dot{E}_{\rm NL}$ turns on as a step function at f_0. Thus by Eq. (4), the cumulative phase shift due to the tide raised in each NS is, according to our model,

$$\Delta\phi(f) = F(M_1, M_2)\frac{A}{n-3} \times \left[\left(\frac{f}{f_{\rm ref}}\right)^{n-3} - \left(\frac{f_0}{f_{\rm ref}}\right)^{n-3}\right]\Theta\left(f - f_0\right), \qquad (7)$$

where we used the point mass quadrupole formula. $F(M_1, M_2)$ is a function of the component masses, and $f_{\rm ref}$ is a reference frequency that sets the dimensionless scale of A. Appendix A provides a more detailed derivation of our model and gives the explicit form of $F(M_1, M_2)$.

Because we do not expect $\dot{E}_{\rm NL}$ to be a particularly strong function of f, we explore values in the range $0 \le n \le 2$. As the binary separation decreases, higher frequency modes become unstable (Equation (1)), which suggests that N and perhaps $E_{\rm sat}$ increase with f, implying $n > 0$. Rapid growth rates suggest that f_0 is of order f_i; we therefore consider values in the range $30 \lesssim f_0 \lesssim 80\,\mathrm{Hz}$ and approximate the "turn-on" behavior with a Heaviside function at f_0. Finally, we consider values of A between 10^{-9} and 10^{-6}. The upper end corresponds approximately to $N \sim 10^3$ modes each saturating at $E_{\rm sat} \sim 10^{-8}E_0$ (corresponding to $\beta \sim 1$ for $\omega_g \sim 10^{-4}\omega_0$; see Equation (5)). At the lower end, the phase shift is too small to be detectable.

The saturation parameters may depend on the stellar structure and thus the component masses. We therefore allow each star in a binary NS system to have its own

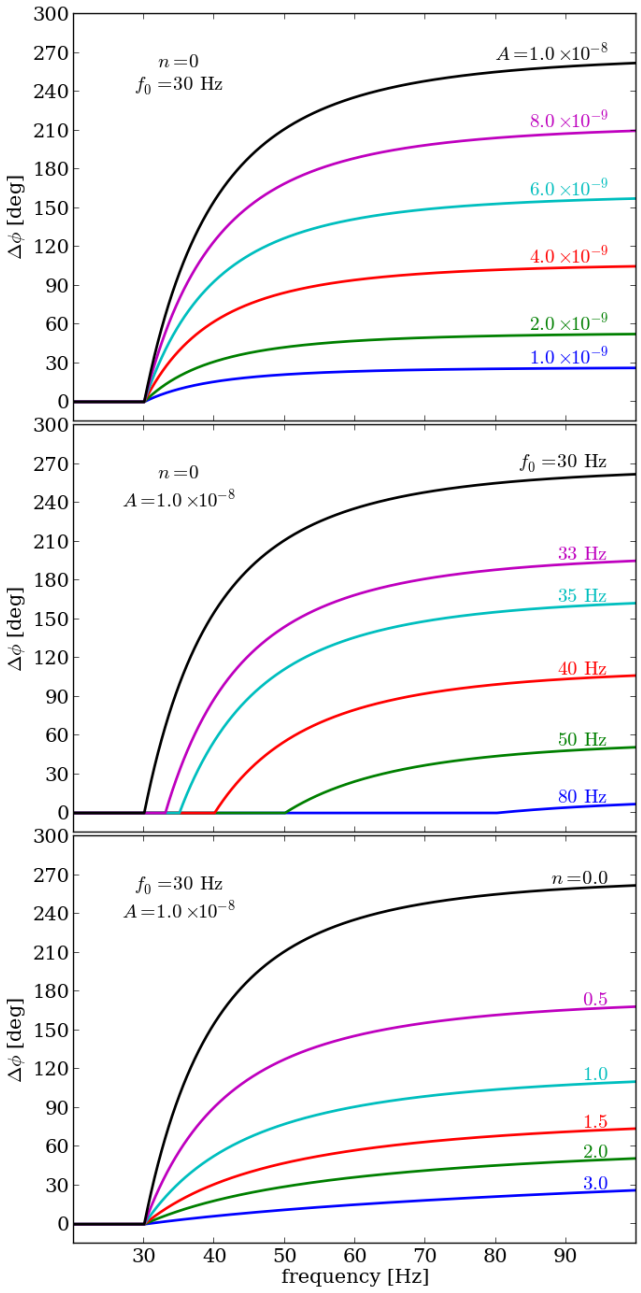

FIG. 2. Cumulative phase shift $\Delta\phi$ as a function of GW frequency f and its dependence on the model parameters A, f_0, and n (top, middle, and bottom panels, respectively).

A, n, and f_0. Following previous work [17], we expand all the parameters around a $1.4M_\odot$ reference mass. For example,

$$A(M_i) \equiv A^{(0)} + A^{(1)}(M_i - 1.4M_\odot) + \cdots \tag{8}$$

and we keep the 0^{th} and 1^{st} order terms. Although we marginalize over both orders, we focus on the 0^{th} order terms throughout this study, dropping the superscript unless otherwise indicated.

In Fig. 1 we show the time domain waveform, with and without the nonlinear corrections to the PP solution, assuming a non-spinning $1.4M_\odot$-$1.4M_\odot$ binary NS system. Although both waveforms are identical at early times ($f < f_0$), a phase shift accumulates throughout the inspiral. For these parameters, the cumulative phase shift at $f \simeq 200$Hz is $\Delta\phi \simeq 200°$. As we show in § V A, the nonlinear tidal effects begin to be detectable at such phase shifts.

In Fig. 2 we show $\Delta\phi(f)$ for a range of A, f_0, and n. Large A implies large total phase shifts $\Delta\phi(f \to \infty)$ whereas large f_0 or n imply the opposite. We also see that although $\Delta\phi(f \to \infty)$ depends on all three parameters, the slope is mostly determined by A and n. Moreover, because we expect $n < 3$, $\Delta\phi$ accumulates most rapidly at low frequencies and asymptotes to a constant value at large frequencies. Since the PP models can account for a constant overall phase shift, detecting the nonlinear tidal effects depends primarily on the low-frequency sensitivity of the detectors.

Assuming a parameterized post-Einsteinian formalism, Cornish et al. [14] study modifications to PP GR waveforms that are, in some ways, similar to ours. In particular, they assume a power-law form for the phase shift, $\Delta\phi(f) \sim Af^n$, and explore a range of power-law amplitudes and exponents. However, they do not include a turn-on frequency f_0. Furthermore, they focus on high frequencies because they find that solar-system tests are more sensitive than GW measurements at low frequencies. Nonetheless, their conclusions are consistent with ours to the extent that they can be compared.

IV. BAYESIAN INFERENCE

We use Bayesian methods to assess how our model of the nonlinear tidal effects impacts the GW data analysis. Specifically, we use Nested Sampling [33, 40] within LALInference [41] to compute posterior distributions and evidences. In the most general PP case, the GW signal emitted by a binary in a circular orbit depends on 15 parameters, including the two component masses, source location, orientation, distance, and six degrees of freedom for the two spins. We collectively refer to the unknown parameters as $\vec{\theta}$. In a Bayesian framework, the evidence Z of data d given a model $\mathcal{H}$ is

$$Z \equiv p(d|\mathcal{H}) = \int d\vec{\theta}\, p(d|\vec{\theta},\mathcal{H}) p(\vec{\theta}|\mathcal{H}), \tag{9}$$

where the first term in the integral is the likelihood and the second is the prior, both of which depend on the model. The multi-dimensional posterior distribution of $\vec{\theta}$ can be written using Bayes' theorem as

$$p(\vec{\theta}|d,\mathcal{H}) = \frac{p(d|\vec{\theta},\mathcal{H}) p(\vec{\theta}|\mathcal{H})}{Z}. \tag{10}$$

Furthermore, if two (or more) competing models are available, odds ratios between pairs of models can be cal-

culated as

$$\mathcal{O}^A_B = \frac{p(\mathcal{H}_A|d)}{p(\mathcal{H}_B|d)} = \frac{p(\mathcal{H}_A)Z_A}{p(\mathcal{H}_B)Z_B}, \tag{11}$$

where the ratio of priors reflects the initial relative belief in each model. We assume that no model is preferred a priori and therefore $\mathcal{O}^A_B \to Z_A/Z_B$.

When the gravitational waveform's shape is known a priori, we use templates to represent the expected signal. These templates are parameterized by $\vec{\theta}$ and form a manifold onto which we project the data. By measuring how well different points on the manifold match the data, we construct posterior distributions for each signal parameter. This is effectively what is done within Equations (9) and (10). However, if the manifold does not accurately capture the full range of possible signals, biases may be introduced. Furthermore, if no point on the manifold represents the data well, we may not be able to recover the signal at all (small Z). This effect, commonly referred to as template mismatch, can occur if the phase shift introduced by nonlinear tides is neglected.

In what follows, we consider two models: $\mathcal{H}_{PP}$ treats the two objects as point particles, whereas $\mathcal{H}_{NL}$ includes nonlinear tidal effects. The $\mathcal{H}_{PP}$ model uses a simple inspiral-only analytic approximant [TaylorF2; 13]. The $\mathcal{H}_{NL}$ model augments the TaylorF2 phase evolution with a tide-induced phase evolution given by Eq. (7).

We focus on a single, optimally-oriented, nonspinning[2] binary NS system, analyzed at different distances, corresponding to network signal-to-noise ratios ($\rho_{\rm net}$) near 12, 25 and 50. These roughly correspond to marginal, confident, and gold-plated detections, respectively. We also neglect linear tides, which we expect to decouple from the NL effects because the former are significant at high frequencies while the latter are most significant at relatively low frequencies (see Fig. 2). We include the LIGO Hanford and Livingston detectors in addition to Virgo [6], assuming expected sensitivities for the second observing run [O2; 4]. While these may not be realized exactly, they should approximate the relative sensitivities of the detectors. Because detections will be driven by the two LIGO instruments, which are expected to be more sensitive than Virgo, we place our signal directly overhead North America [4]. Virgo will mostly improve localization through triangulation but will not significantly influence our ability to constrain intrinsic parameters. Finally, we use a zero-noise realization for our simulations, which is equivalent to taking the expected value of the evidence and posterior distributions from many noise realizations [38]. Details of our priors on all parameters are provided in Appendix B.

[2] We briefly consider aligned spins in § V A.

V. DETECTABILITY AND BIASES WHEN NONLINEAR TIDES ARE NEGLECTED

We begin by investigating the impact of neglecting nonlinear tidal effects. We do this by injecting signals that include the tide-induced phase shift but then fit the data using only the PP waveforms. This causes significant template mismatch if the tidal effects are large, impairing our ability to detect events and biasing the inferred parameters.

Detectability and bias are related but subtly different. For example, the best fit may not be very good but nevertheless remain near the true parameters (i.e., unbiased but impaired detection). Alternatively, we may be able to find a good fit but only with parameters that are far from the true values (i.e., biased but unimpaired detection). Depending on the magnitude of $\Delta\phi$ and its frequency evolution, we observe one or both effects.

A. Detectability

As $\Delta\phi$ increases, the template mismatch worsens. We generally find that when $A \gtrsim 10^{-8}$ nonlinear tidal effects begin to be noticeable for current detector sensitivities. From Fig. 2, we see that this corresponds to $\Delta\phi \gtrsim 1$ radian, which is similar to other estimates of the minimum measureable $\Delta\phi$ (see, e.g., [10, 15]). In terms of the saturation model described in § III, $A \gtrsim 10^{-8}$ corresponds to, e.g., $N \sim 10$ unstable modes saturating at $E_{\rm sat} \sim E_{\rm break}$ or equivalently $N \sim 10^3$ modes saturating at $E_{\rm sat} \sim 0.01 E_{\rm break}$.

We illustrate this result in Fig. 3 for signals that include nonlinear tidal effects injected with $\rho_{\rm net} \simeq 25$. We show the odds ratio $\mathcal{O}^{PP}_N$ of a PP waveform model relative to pure Gaussian noise as a function of A for different values of n and f_0. For small A, $\mathcal{O}^{PP}_N$ plateaus at large values because the PP signal model matches the data well. However, as A increases the PP model matches the data less and less, thereby decreasing the evidence for the existence of a signal. $\mathcal{O}^{PP}_N$ can be mapped into the recovered $\rho_{\rm net}$ (called $\rho_{\rm rec}$), and we see that for $A \sim 10^{-6}$ more than half of the signal is lost ($\rho_{\rm rec} < \rho_{\rm net}/2$). At such a signal loss, we would miss more than $1 - (1/2)^3 \simeq 90\%$ of NS merger events. For $\rho_{\rm net} \simeq 12$, extreme values of A can produce $\mathcal{O}^{PP}_N < 1$, which implies that Gaussian noise is preferred over the PP signal model even though we use a zero-noise realization. All $\rho_{\rm net}$ produce nearly identical curves and simply scale $\mathcal{O}^{PP}_N$ up or down. Signal loss due to template mismatch produces this behavior because we lose a fixed fraction of the inner product between the template and the data regardless of the overall amplitude.

As Fig. 3 shows, the decrease of $\mathcal{O}^{PP}_N$ with increasing A depends only mildly on n and f_0. We can see this in more detail in Figure 4, which shows $\mathcal{O}^{PP}_N$ as a function of n and f_0 for two values of A. Typically, small n imply more rapid accumulation of phase shift and small f_0 im-

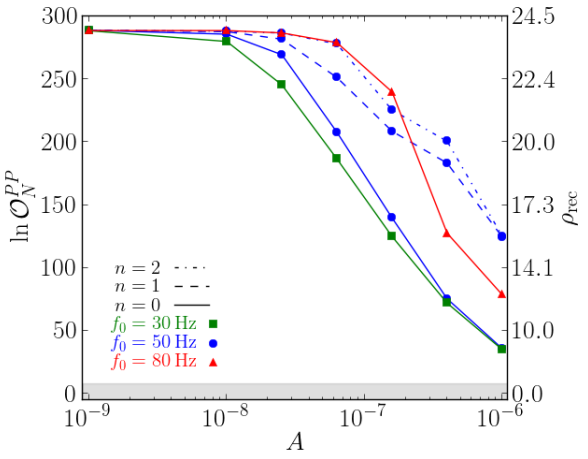

FIG. 3. $\mathcal{O}_N^{PP}$ for injected signals that include nonlinear tidal effects but are recovered using PP waveforms. The signals are injected at $\rho_{\rm net} \simeq 25$. The right axis shows the recovered signal-to-noise ratio $\rho_{\rm rec}$, computed from $\mathcal{O}_N^{PP}$ in the Laplace approximation as $\mathcal{O}_N^{PP} = \rho_{\rm rec}^2/2$.

ply more total phase shift, both of which produce larger template mismatch and lower $\mathcal{O}_N^{PP}$. However, we note that $\mathcal{O}_N^{PP}$ for high f_0 injections depends more strongly on A than low f_0 injections.

1. *Effects of spin*

We also briefly investigated the effects of spins with TaylorF2 approximants. These signals allow the components to spin either aligned or anti-aligned with the orbital angular momentum, and therefore do not include precession effects. Spins can change the waveform's duration, which may be confused with the analogous effect from nonlinear tidal interactions. Searches often use TaylorF2 for low-mass systems involving NSs and restrict themselves to only relatively small spins (dimensionless spin parameters $|\chi_{1,2}| \leq 0.05$). Nonetheless, we performed a grid-based calculation to determine the possible improvements in detectability provided by spins, extending our search to $|\chi_{1,2}| \leq 0.1$. We find that including spins only marginally increases $\rho_{\rm rec}/\rho_{\rm net}$ (e.g., from 0.30 to 0.34 for $A = 10^{-6}$). The slight improvement is likely due to spins compensating somewhat at high frequencies for the biases in $\mathcal{M}$ induced at low frequencies by the NL effects (see § V B). If this is the case, measurements of the spin may be biased, which has implications for population synthesis inferences [1].

Full spinning waveforms may increase the match further, but it is unlikely that they will recover a significant fraction of the "lost" $\rho_{\rm net}$. We conclude that spin may be important for studies of populations of marginally detectable sources with marginally relevant values of A, but it should not significantly change the implications of this study. When A is large, we see a dramatic reduction in our ability to recover signals even when using spinning PP waveforms.

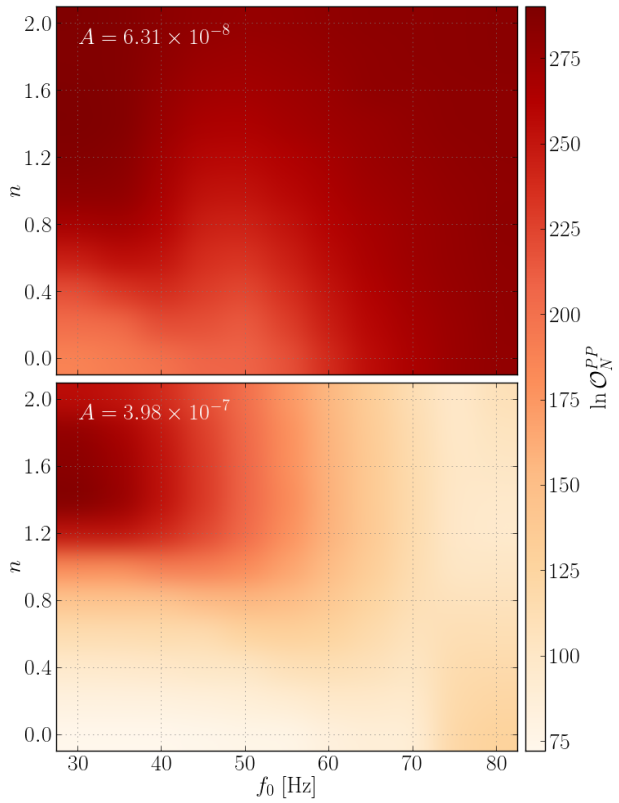

FIG. 4. Surface plots of $\mathcal{O}_N^{PP}$ as a function of n and f_0 at $A = 6.31 \times 10^{-8}$ (top panel) and $A = 3.98 \times 10^{-7}$ (bottom panel). The signals are injected at $\rho_{\rm net} \simeq 25$.

B. Biases

When A is small, PP models fit the true waveform well and the posterior distributions are centered on the true values. At $A \sim 10^{-8}$ we begin to observe biases in the recovered parameters even though $\mathcal{O}_N^{PP}$ has decreased by only a few percent. This is sometimes called a "stealth bias" [14, 39]. Figure 5 shows the joint and marginal posterior distributions of the chirp mass ($\mathcal{M} = (M_1 M_2)^{3/5}/(M_1 + M_2)^{1/5}$) and the mass ratio ($q = M_2/M_1$) as a function of A for $n = 0$, $f_0 = 50$ Hz with $\rho_{\rm net} \simeq 25$. We observe a clear bias in $\mathcal{M}$ as A increases. This is because larger A imply faster orbital decay, which can be confused with heavier systems that also decay faster. Even at $A = 10^{-8}$, we observe a statistically significant bias in $\mathcal{M}$ even though $\mathcal{O}_N^{PP}$ is essentially identical to the $A = 0$ result. Therefore, nonlinear tidal effects can bias parameter estimation even before they impact detection. However, we note that although the bias in $\mathcal{M}$ can be much larger than the statistical uncertainty, in absolute terms it remains small even for extreme values of A.

Nonlinear tides also introduce biases in the mass ratio q, particularly when the impact on detectability is marginal. For $A \lesssim 5 \times 10^{-8}$, q is biased toward more asymmetric component masses. This is because asymmetric systems also decay faster. In fact, for large f_0, q is biased so much that $\mathcal{M}$ is inferred to be *smaller* than it really is (see Appendix C). For our $1.4M_\odot$-$1.4M_\odot$ system, we find that at $A \sim$ few$\times 10^{-8}$ the larger mass may be inferred to be as much as $1.6M_\odot$ and the smaller mass as little as $1.2M_\odot$ (red curve in Fig. 5). For different values of n, the bias in q can be even more extreme than this. However, we are not likely to misclassify a NS-NS binary as a NS-BH system unless perhaps one NS is near the maximal mass.

As Fig. 5 shows, the bias in q is large for intermediate values of $A \sim 10^{-8}$ but small for $A \ll 10^{-8}$ and $A \gg 10^{-8}$. By contrast, we find that the bias in $\mathcal{M}$ increases nearly monotonically with A. Apparently, for $A \lesssim 10^{-8}$, which corresponds to $\Delta\phi \lesssim 1$ radian, the PP model can still approximate the data reasonably well, but only with a substantially biased q. We find that this trend holds for all values of f_0 and n. However, for $A \gg 10^{-8}$, $\mathcal{O}_N^{PP}$ decreases significantly and, even though no set of PP parameters captures the data well, the true parameter values again offer the best fit (with the exception of $\mathcal{M}$, which remains biased at large A).

Despite the potential for biases, the posteriors for the component masses M_1 and M_2 almost always have some support near the true value, even if it corresponds to a long tail relative to the mode of the distribution. We also find that heavier systems or systems with small q (including NS-BH systems) are less biased by NL effects. This is because they decay faster and spend less time in the slow inspiral phase where nonlinear tides make their greatest impact. Quantitatively, this effect is captured by the function $F(M_1, M_2)$ in Eq. (7).

Nonlinear tides can also bias the luminosity distance D_L. In Fig. 6 we show the posterior distribution of D_L and orbital inclination θ_{jn}. As we showed above, the PP model compensates for increasing A by increasing $\mathcal{M}$. However, systems with larger $\mathcal{M}$ are intrinsically more luminous and therefore are inferred to come from larger D_L. Despite the bias, we find that the posterior distribution of D_L is always broad enough to cover the true value.

The other extrinsic parameters, such as θ_{jn} and source position, are unbiased by nonlinear tides. This is because the phase shift affects both polarizations equally and these other extrinsic parameters depend primarily on the ratio of the two polarizations. Although not biased, the decrease in $\mathcal{O}_N^{PP}$ with increasing A does broaden the posteriors of all extrinsic parameters.

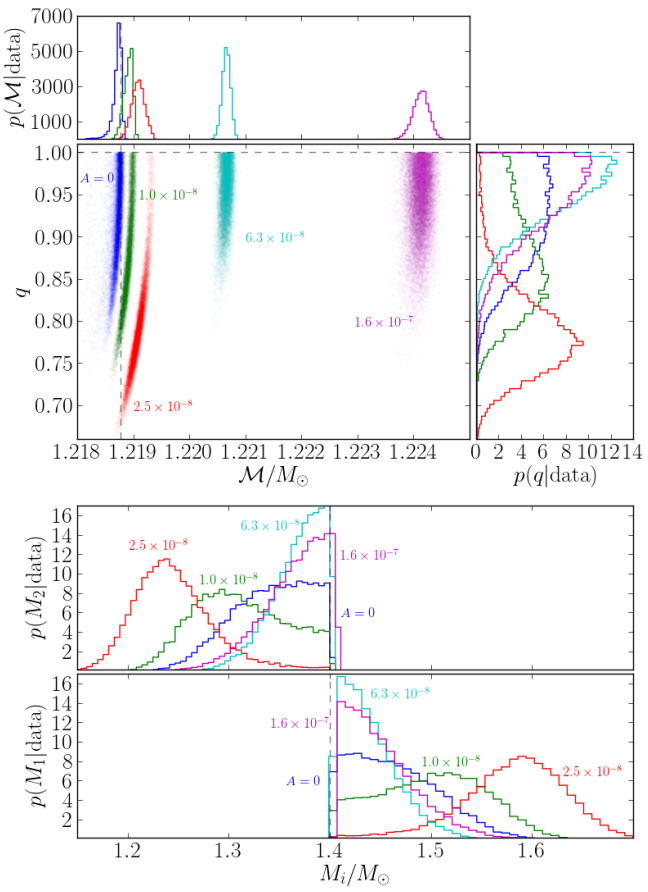

FIG. 5. (top) Joint and marginal posterior distributions of $\mathcal{M}$ and q for injected signals that include nonlinear tidal effects but are recovered using PP waveforms. (bottom) Marginal distributions for the individual component masses, which are restricted to $M_1 \geq M_2$. The different curves show results for different values of A. We take $f_0 = 50\,\mathrm{Hz}$ and $n = 0$, and inject the signals at $\rho_{\mathrm{net}} \simeq 25$.

VI. MEASURABILITY AND MODEL SELECTION WITH NONLINEAR TIDES

Having quantified the impact of neglecting nonlinear tidal effects in § V, we now consider how well they can be measured when they are included in the analysis. In § VI A we evaluate the statistical evidence for their existence and in § VI B we assess how well we can constrain the nonlinear tide parameters from the data. To do this, we repeat the simulations in § V but now use a model that *does* include the nonlinear effects when recovering the signal. We thereby obtain posterior distributions for A, n, and f_0 as well as odds ratios $\mathcal{O}_N^{NL}$comparing the nonlinear tide model to Gaussian noise.

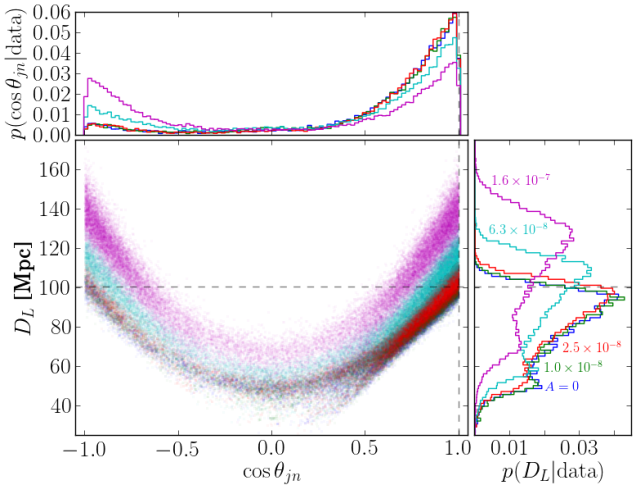

FIG. 6. Joint and marginal posterior distribution for luminosity distance D_L and inclination θ_{jn} for injected signals that include nonlinear tidal effects but are recovered using PP waveforms. We take $f_0 = 50\,\text{Hz}$, and $n = 0$, and inject the signals at $\rho_{\rm net} \simeq 25$, corresponding to $D_L \simeq 100$ Mpc.

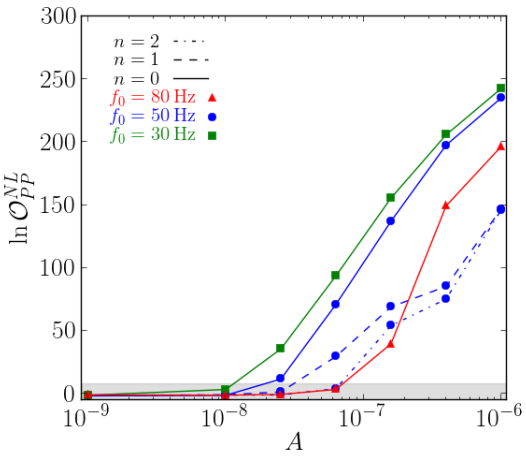

FIG. 7. $\mathcal{O}^{NL}_{PP}$ for the same parameters as Fig. 3.

A. Model selection

By computing both $\mathcal{O}^{PP}_N$ and $\mathcal{O}^{NL}_N$, we obtain an odds ratio comparing the two signal models $\ln\mathcal{O}^{NL}_{PP} = \ln\mathcal{O}^{NL}_N - \ln\mathcal{O}^{PP}_N$. This provides a statistical measure of the evidence for each model. If $\mathcal{O}^{NL}_{PP}$ is large, the nonlinear (NL) model is favored.

In Figure 7 we show $\mathcal{O}^{NL}_{PP}$ as a function of A. For $A \lesssim 10^{-8}$, we find $\mathcal{O}^{NL}_{PP} < 1$ which implies that the model neglecting nonlinear tides is favored. This is due to Occam's razor, which penalizes the more complicated models that include nonlinear tides, because they do not match the data significantly better than the simpler models that ignore them. Typically, the Occam factor corresponds to $\ln\mathcal{O}^{NL}_{PP} \sim -0.1$ and is not strongly dependent on $\rho_{\rm net}$. For $\rho_{\rm net} \simeq 25$, this corresponds to less than 0.05% of $\mathcal{O}^{PP}_N$. However, when $A \gtrsim 10^{-8}$, the NL models are strongly favored. Comparing with Fig. 3, we see that $A \sim 10^{-8}$ is also where $\mathcal{O}^{PP}_N$ begins to decrease. This is not a coincidence. The NL models are able to reconstruct the signal equally well regardless of A and $\mathcal{O}^{NL}_N \simeq$ constant. Therefore, $\ln\mathcal{O}^{NL}_{PP} \simeq$ constant $- \ln\mathcal{O}^{PP}_N$ and the critical values of A for detectability and model selection are the same. Figure 8 shows that the trend continues as a function of n and f_0 as well. Figures 8 and 4 are inverses; areas that were 'hot' become 'cold' and vice versa. Therefore, the regions of parameter space where the PP models fail correspond (perhaps unsurprisingly) to the regions where the models with nonlinear tides are most favored. It also means that we can recover all of the $\rho_{\rm net}$ that is "lost" when nonlinear tides are neglected by using a more complete model.

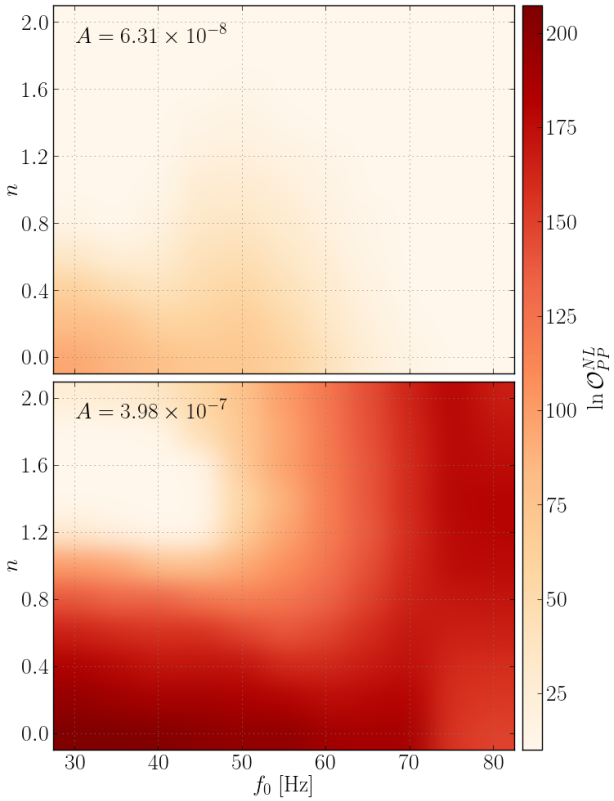

FIG. 8. Surface plots of $\mathcal{O}^{NL}_{PP}$ as a function of n and f_0 at (top panel) $A = 6.31\times10^{-8}$ and (bottom panel) $A = 3.98\times10^{-7}$. The signals are injected at $\rho_{\rm net} \simeq 25$.

1. *Tests of GR (with only linear tides)*

While it is clear that we can distinguish NL models from PP models for large A, it is also interesting to consider whether we can detect deviations from the PP model without the correct alternative model. TIGER [8, 27, 28] is designed to answer exactly this ques-

tion and computes odds ratios between the PP model and generic deviations from vacuum GR ($\mathcal{O}^{!PP}_{PP}$). It does so by allowing the post-Newtonian (PN) coefficients to vary away from their GR predictions and computing evidences for the modified models. Furthermore, TIGER is agnostic about the effects of linear tides and only considers $f \lesssim 400$Hz [9]. In this way, it focuses on the early inspiral alone, during which the PP model is expected to be correct. We ran TIGER over a single event ($A = 1.6\times10^{-7}$, $f_0 = 50\,\mathrm{Hz}$, $n = 2$) and observed large evidences for models allowing the first four PN coefficients to vary. They correspond to $\ln \mathcal{O}^{!PP}_{PP} \simeq 45$ when $\rho_{\rm net} \simeq 25$ and strong evidence in favor of the alternative hypothesis. By comparison, the same injection corresponds to $\ln \mathcal{O}^{NL}_{PP} \simeq 53$. We also note that $n = 2$ corresponds to some of the smaller $\mathcal{O}^{NL}_{PP}$ observed, and other parameters are likely to produce even larger evidences in favor of TIGER's alternative hypothesis.

Various studies have shown TIGER to be insensitive to most uncertainties associated with compact binary coalescences and interferometric observatories (e.g., linear tides and calibration uncertainties) [7, 8]. However, we find that nonlinear tide effects, if large and ignored, can fool the TIGER machinery and suggest that GR is not the correct theory of gravity when, in fact, GR is the correct theory and we have simply neglected relevant physics within the NSs. To our knowledge, this is the first example of an effect that, if ignored, could fool TIGER. This therefore stresses the implicit assumption within the TIGER analysis that all relevant physics has already been included in the model. We also note that we only processed a single event with TIGER, but the results are suggestive nonetheless.

B. Measureability

We found that neglecting nonlinear tides when $A \gtrsim 10^{-8}$ can significantly hamper detection and bias parameter estimation. Conversely, we found that if $A \gtrsim 10^{-8}$, there will be strong statistical evidence for nonlinear tides. We now consider how well we can constrain the nonlinear parameters with data from a single event.

We first evaluate what upper bound on A is achieved when nonlinear effects are extremely small (i.e., for injected signals with $A \to 0$). In Fig. 9 we show the posterior distributions of A for different values of $\rho_{\rm net}$ assuming a uniform prior for $\log A$. We find that the upper bound is near $A \sim 10^{-8}$, with a slight decrease with increasing $\rho_{\rm net}$. This is not surprising given that at this A the tidal effects begin to be noticeable (§ V).

In Figure 10 we show the marginal posterior distributions for A, n, and f_0 for injections at $\rho_{\rm net} \simeq 25$. When $A \lesssim 10^{-8}$, we cannot measure n or f_0. However, for $A \gtrsim 10^{-8}$, we can measure both n and f_0 to relatively high precision even at $\rho_{\rm net} \sim 12$. Typically, we measure A and f_0 comparably, based on a comparison of the Kullback-Leibler divergence from the prior to the posterior and the entropy of the posteriors. Measuring n, however, requires either larger A or $\rho_{\rm net}$.

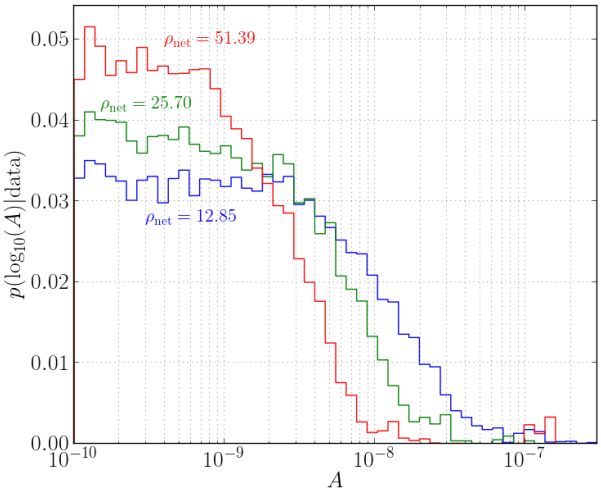

FIG. 9. Posterior distributions for A when the injected signal does not include nonlinear tide effects.

There are also degeneracies between many of the parameters in our model. The strongest degeneracy is between A and $\mathcal{M}$, which we show in Fig. 11. When $A \sim 10^{-8}$ and nonlinear tides are marginally detectable we find a negative correlation between $\mathcal{M}$ and A (larger $\mathcal{M}$ favor smaller A and vice versa; green points in Fig. 11). This is because a bias towards larger $\mathcal{M}$ shortens the inspiral and thereby mimics the effects of the nonlinear tide. When $A \gtrsim 10^{-8}$, the degeneracy between $\mathcal{M}$ and A is present but truncated because $A \ll 10^{-8}$ is ruled out.

We also find degeneracies between the nonlinear parameters. A has a strong positive correlation with n because $\Delta\phi \propto A/(n-3)$. Interestingly, this forces A to have a weak negative correlation with f_0 because larger A imply larger n, which then requires a smaller f_0 to maintain roughly the same $\Delta\phi$. However, this correlation breaks down for large f_0, because $\Delta\phi$ then depends more strongly on f_0, weakening the correlation between n and A and strengthening the correlation between f_0 and A.

1. *Dependence on component mass*

So far, we have focused on only the leading order terms in our Taylor expansions of A, f_0, and n (see Equation 8). However, our reconstructions also sampled the $1^{\rm st}$ order terms. We do not find any strong correlations between the $0^{\rm th}$ and $1^{\rm st}$ order terms. Nonetheless, while most marginal posterior distributions for the $1^{\rm st}$ order terms are completely unconstrained, occasionally we observe weak constraints on df_0/dm near the boundary of its prior.

If this result holds more generally and we are able to measure f_0 as a function of component mass from a series

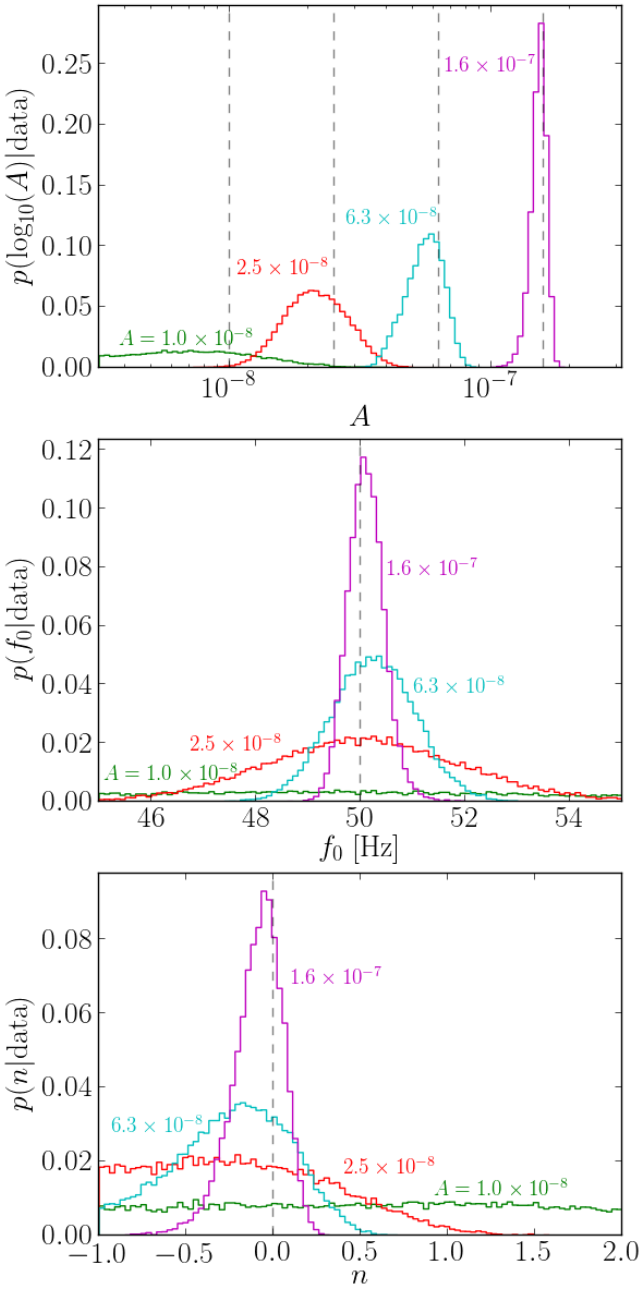

FIG. 10. Measurability of (top) A, (middle) f_0, and (bottom) n as a function of A. Vertical dashed lines show injected values. We take $f_0 = 50\,\text{Hz}$ and $n = 0$, and inject the signals at $\rho_{\text{net}} \simeq 25$.

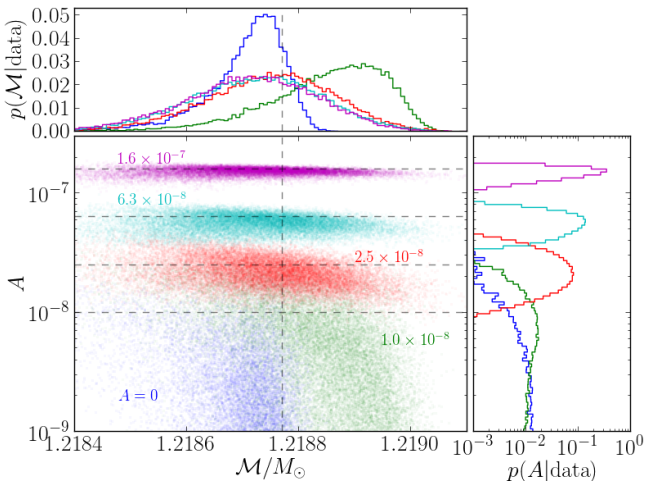

FIG. 11. Joint and marginal posterior distributions of $\mathcal{M}$ and A for various values of A. We take $f_0 = 50\,\text{Hz}$ and $n = 0$, and inject the signals at $\rho_{\text{net}} \simeq 25$.

of detections, we may be able to use f_0 to make cosmological measurements using GWs alone. This is because f_0 provides an intrinsic frequency scale that gives a handle on the redshift of the otherwise conformal inspiral. Indeed, if we can measure f_0 as a function of mass, we may extract both the redshift and the luminosity distance directly from the GW signal without recourse to an electromagnetic counterpart. Further studies will be needed, however, to test this idea and to evaluate the robustness of our saturation model.

We also carried out analyses in which we allow each body to have independent values of A, f_0, and n (as an alternative to the Taylor series expansions in component mass). Because there is a relatively weak dependence on mass ratio q in the phase shift (Appendix A) and because binary NS systems should have $q \sim 1$, we find a strong degeneracy between A_1 and A_2. Generally, the posterior supports large A for one mass and small A for the other, disfavoring nearly equal A for both masses (even if the masses are similar). The Taylor expansion approach, by contrast, ensures similar values of A for similar mass NSs. We therefore consider it a better method. Most importantly, the weak constraints placed on the 1^{st} order terms suggests that we capture most of the nonlinear tidal effects with just the 0^{th} order terms.

VII. SUMMARY AND CONCLUSIONS

By constructing a parameterized model of the saturation of the p-g instability in coalescing binary NSs, we explored how the instability might impact GW signals for current detector sensitivities. Our model contains three parameters (A, f_0, and n), where A and n determine the magnitude and frequency dependence of the nonlinear dissipation rate $\dot{E}_{\text{NL}}$, and f_0 is the GW frequency at which the unstable modes saturate. Applying a full Bayesian analysis, we determined as a function of A, f_0, and n the extent to which nonlinear tidal effects: (1) influence the detectability of merger events, (2) bias binary parameters such as the chirp mass $\mathcal{M}$, the mass ratio q, the component masses, and the luminosity distance D_L, and (3) can be measured. We also examined, albeit in less detail, how the instability might be confused with NS spin and generic deviations from vacuum GR when a

point-particle model is assumed at low frequencies.

We find that neglecting nonlinear tidal effects can significantly impair our ability to detect events. For example, if $A \sim 10^{-7}$, $n = 0$, and $f = 50$ Hz, we would lose $\simeq 30\%$ of $\rho_{\rm net}$. This means that if we neglect nonlinear tides, we would miss $1 - (0.70)^3 \simeq 70\%$ of NS merger events. More generally, we find that nonlinear effects are detectable if $A \gtrsim 10^{-8}$. An $A \sim 10^{-8}$ yields a phase shift relative to the PP waveform of $\Delta\phi \sim 1$ radian and corresponds to $N \sim 10$ and $E_{\rm sat} \sim E_{\rm break}$ or $N \sim 10^3$ and $E_{\rm sat} \sim 10^{-2} E_{\rm break}$. Although N and $E_{\rm sat}$, and therefore A, are highly uncertain, values as large as $A \sim 10^{-6}$ and thus $\Delta\phi \sim 10^2$ radian are a possibility (see § II and § III). We also note that if $A \sim 10^{-6}$, $n = 0$, and $f = 50$ Hz, and we neglect nonlinear tides, we would miss $\simeq 95\%$ of NS merger events. On the other hand, if $A \ll 10^{-8}$ (e.g., $E_{\rm sat} \ll E_{\rm break}$ and $N \sim 1$), nonlinear tidal effects will be completely unimportant for current detectors.

We also found that intrinsic parameter biases can be significant if nonlinear tidal effects are neglected. For example, we found that for $A \sim$ few $\times 10^{-8}$, a $1.4M_\odot - 1.4M_\odot$ NS binary would be strongly biased to $1.6M_\odot - 1.2M_\odot$. Interestingly, at this A the loss in signal $\rho_{\rm net}$ is relatively mild ($\lesssim 10\%$) and the PP waveform model would appear to be a good match to the data, an example of a "stealth bias". For larger A, the biases in many of the parameters tend to actually *decrease* with increasing A (the bias in $\mathcal{M}$ does not follow this pattern, however). Nonetheless, the quality of the PP model match always worsens with increasing A.

We also investigated whether we can detect deviations from the PP model without knowing the form of the nonlinear effects. In particular, TIGER detects deviations from the PP model if A is large. Although the evidence in favor of TIGER's alternative hypothesis is less than the evidence in favor of the exact nonlinear model, it does provide a significantly better match than the PP model. This suggests that we may not need to know the precise form of the nonlinear effects in order to improve the match to the data. This also highlights the fact that neglected physics within NSs could be confused for evidence that GR is not the correct theory of gravity.

For heavier systems, such as NS-BH systems, nonlinear effects are significantly less important. This is because these systems are intrinsically more luminous and decay faster, giving the nonlinear tides less time to modify the inspiral. Therefore, for the same A, f_0, and n, their waveform phase shifts are much smaller.

Assuming that we observe a cosmological population of sources, nonlinear tides may provide a way to extract distance-redshift information directly from GW waveforms without identification of an electromagnetic counterpart. This is because they provide a characteristic frequency (f_0) that breaks the otherwise conformal waveform. By measuring f_0, we can extract the redshift directly and associate it with the corresponding D_L. Other studies of tidal effects have suggested similar approaches [29]. However, we will probably need to tightly constrain the possible values of f_0 a priori in order to make such cosmological measurements.

Lastly, we note that a first-principles calculation of the saturation should be very valuable. It would reduce the large uncertainties in A, f_0, and n and help further assess the potential impact of nonlinear tides. It might also aid parameter estimation and detection pipelines by reducing the amount of parameter space that must be searched. Although a full saturation calculation would be ideal, even relatively small improvements could be useful, such as confirming the expected growth rates of the p-g instability or more accurately determining what sets the lower bound on ω_g and thus the instability threshold.

VIII. ACKNOWLEDGMENTS

The authors would like to thank Scott Hughes for useful discussions and encouragement throughout this project as well as Chris Van Der Broek, Michalis Agathos, and Richard O'Shaughnessy for their comments and suggestions on the draft. R.E. and N.W. were supported in part by NASA ATP grant NNX14AB40G. The authors also acknowledge the support of the National Science Foundation and the LIGO Laboratory. LIGO was constructed by the California Institute of Technology and Massachusetts Institute of Technology with funding from the National Science Foundation and operates under cooperative agreement PHY-0757058. The authors would like to acknowledge the LIGO Data Grid clusters. Specifically, we thank the Albert Einstein Institute in Hannover, supported by the Max-PlanckGesellschaft, for use of the Atlas high-performance computing cluster.

[1] Abbott, B. P., Abbott, R., Abbott, T. D., et al. 2016, The Astrophysical Journal Letters, 818, L22
[2] —. 2016, Phys. Rev. Lett., 116, 241103
[3] —. 2016, Phys. Rev. Lett., 116, 061102
[4] Abbott, B. P., Abbott, R., Abbott, T. D., et al. 2016, Living Reviews in Relativity, 19, arXiv:1304.0670
[5] Abbott, B. P., Abbott, R., Abbott, T. D., et al. 2016, Phys. Rev. Lett., 116, 221101
[6] Acernese, F., Agathos, M., Agatsuma, K., et al. 2015, Classical and Quantum Gravity, 32, 024001
[7] Agathos, M., Del Pozzo, W., Li, T. G. F., et al. 2013, ArXiv e-prints, arXiv:1305.2963
[8] Agathos, M., Del Pozzo, W., Li, T. G. F., et al. 2014, Phys. Rev. D, 89, 082001
[9] Agathos, M., Meidam, J., Del Pozzo, W., et al. 2015, Phys. Rev. D, 92, 023012

[10] Balachandran, P., & Flanagan, E. E. 2007, ArXiv General Relativity and Quantum Cosmology e-prints, gr-qc/0701076
[11] Barker, A. J. 2011, mnras, 414, 1365
[12] Barker, A. J., & Ogilvie, G. I. 2010, Monthly Notices of the Royal Astronomical Society, 404, 1849
[13] Buonanno, A., Iyer, B. R., Ochsner, E., Pan, Y., & Sathyaprakash, B. S. 2009, Phys. Rev. D, 80, 084043
[14] Cornish, N., Sampson, L., Yunes, N., & Pretorius, F. 2011, Phys. Rev. D, 84, 062003
[15] Cutler, C., & Flanagan, É. E. 1994, Phys. Rev. D, 49, 2658
[16] Damour, T., Nagar, A., & Villain, L. 2012, Phys. Rev. D, 85, 123007
[17] Del Pozzo, W., Li, T. G. F., Agathos, M., Van Den Broeck, C., & Vitale, S. 2013, Phys. Rev. Lett., 111, 071101
[18] Essick, R., & Weinberg, N. N. 2016, The Astrophysical Journal, 816, 18
[19] Favata, M. 2014, Physical Review Letters, 112, 101101
[20] Flanagan, É. É., & Racine, É. 2007, Phys. Rev. D, 75, 044001
[21] Hinderer, T., Lackey, B. D., Lang, R. N., & Read, J. S. 2010, Phys. Rev. D, 81, 123016
[22] Hinderer, T., Taracchini, A., Foucart, F., et al. 2016, Physical Review Letters, 116, 181101
[23] Ho, W. C. G., & Lai, D. 1999, Monthly Notices of the Royal Astronomical Society, 308, 153
[24] Lackey, B. D., & Wade, L. 2015, Phys. Rev. D, 91, 043002
[25] Lai, D. 1994, Monthly Notices of the Royal Astronomical Society, 270, 611
[26] Lai, D., & Wu, Y. 2006, Phys. Rev. D, 74, 024007
[27] Li, T. G. F., Del Pozzo, W., Vitale, S., et al. 2012, Phys. Rev. D, 85, 082003
[28] Li, T. G. F., Pozzo, W. D., Vitale, S., et al. 2012, Journal of Physics: Conference Series, 363, 012028
[29] Messenger, C., & Read, J. 2012, Phys. Rev. Lett., 108, 091101
[30] Read, J. S., Markakis, C., Shibata, M., et al. 2009, Phys. Rev. D, 79, 124033
[31] Read, J. S., Baiotti, L., Creighton, J. D. E., et al. 2013, Phys. Rev. D, 88, 044042
[32] Reisenegger, A., & Goldreich, P. 1994, Astrophys. J., 426, 688
[33] Skilling, J. 2006, Bayesian Anal., 1, 833
[34] Staquet, C., & Sommeria, J. 2002, Annual Review of Fluid Mechanics, 34, 559
[35] Steinhoff, J., Hinderer, T., Buonanno, A., & Taracchini, A. 2016, ArXiv e-prints, arXiv:1608.01907
[36] The LIGO Scientific Collaboration, Aasi, J., Abbott, B. P., et al. 2015, Classical and Quantum Gravity, 32, 074001
[37] The LIGO Scientific Collaboration, the Virgo Collaboration, Abbott, B. P., et al. 2016, ArXiv e-prints, arXiv:1606.04856
[38] Vallisneri, M. 2008, Phys. Rev. D, 77, 042001
[39] Vallisneri, M., & Yunes, N. 2013, Phys. Rev. D, 87, 102002
[40] Veitch, J., & Vecchio, A. 2010, Phys. Rev. D, 81, 062003
[41] Veitch, J., Raymond, V., Farr, B., et al. 2015, Phys. Rev. D, 91, 042003
[42] Venumadhav, T., Zimmerman, A., & Hirata, C. M. 2014, The Astrophysical Journal, 781, 23
[43] Weinberg, N. N. 2016, The Astrophysical Journal, 819, 109
[44] Weinberg, N. N., Arras, P., & Burkart, J. 2013, The Astrophysical Journal, 769, 121
[45] Weinberg, N. N., Arras, P., Quataert, E., & Burkart, J. 2012, Astrophys. J., 751, 136
[46] Yagi, K., & Yunes, N. 2014, Phys. Rev. D, 89, 021303

Appendix A: Phase shift due to the nonlinear tide

We compute the tidal phase shift $\Delta\phi(f)$ relative to the non-spinning PP model using a $0^{\rm th}$ order post-Newtonian (PN) expansion. We expect that higher order PN terms will simply add to the PP result without significantly modifying the effects from nonlinear tidal interactions. Moreover, any correction from higher order PN terms will be small compared to the $0^{\rm th}$ order term since the effects we consider occur predominantly at low frequencies ($f \lesssim 100\,{\rm Hz}$).

We assume a circular, quasi-Keplerian orbit that loses energy due to gravitational radiation and dissipative tidal interactions (between star 1 and star 2)

$$\dot{E}_{\rm orb} = -\dot{E}_{\rm gw} - \dot{E}_1 - \dot{E}_2, \tag{A1}$$

where

$$\dot{E}_{\rm orb} = -\frac{G^{2/3}\pi^{2/3}\mathcal{M}^{5/3}\dot{f}}{3f^{1/3}},$$

$\mathcal{M} = (M_1M_2)^{3/5}/(M_1+M_2)^{1/5}$ is the chirp mass, $f = \Omega/\pi$ is the GW frequency, $\Omega = [G(M_1+M_2)/a^3]^{1/2}$ is the Keplerian frequency, and

$$\dot{E}_{\rm gw} = \frac{32\pi^{10/3}}{5}\frac{G^{7/3}\mathcal{M}^{10/3}}{c^5}f^{10/3}.$$

We model the dissipation due to the tide raised in M_1 by M_2 as

$$\dot{E}_1 = \Gamma_1 N_1 E_{\rm sat,1}$$

(and similarly for the tide raised in M_2 if both are NSs), where Γ is the growth rate of the instability, N the number of unstable modes, and $E_{\rm sat}$ the energy at which the unstable modes saturate. As we describe in § II,

$$\Gamma_1 = 2\lambda_1\epsilon_1\omega_{0,1} = 2\lambda_1\frac{M_2}{M_1}\left(\frac{R_1}{a}\right)^3\omega_{0,1},$$

$$E_{\rm sat,1} = \beta_1 E_{\rm break,1} = \beta_1\left(\frac{\omega_{g,1}}{\Lambda_{g,1}\omega_{0,1}}\right)^2 E_{0,1},$$

where $\omega_0^2 = GM/R^3$ and $E_0 = GM^2/R$. Thus,

$$\dot{E}_1 = 2\pi^2\frac{M_1M_2}{M_1+M_2}(GM_1)^{2/3} \times\left[\omega_{0,1}^{-1/3}\left(\frac{\omega_{g,1}}{\Lambda_{g,1}\omega_{0,1}}\right)^2\beta_1N_1\lambda_1\right]f^2. \tag{A2}$$

As the orbit decays, the fraction of the breaking amplitude at which the instability saturates (β) may increase and there may be more unstable modes (N). Therefore, we expect these parameters to vary with frequency and for simplicity we assume

$$\beta_1 N_1 \lambda_1 = [\beta_1 N_1 \lambda_1]_{\rm ref} \left(\frac{f}{f_{\rm ref}}\right)^{n_1} \Theta_1,$$

i.e., a power law dependence with a sudden onset of the dissipation at $f = f_{0,1}$ as captured by the Heaviside function $\Theta_1 = \Theta(f - f_{0,1})$ (the latter assumption is motivated by the rapid growth rates relative to the inspiral rate as described in § 5.4 of W16). We define the magnitude of $\beta_1 N_1 \lambda_1$ relative to the value at an arbitrary reference frequency $f_{\rm ref}$. In the numerical results below we set $f_{\rm ref} = 100$ Hz (for both star 1 and star 2). Then

$$\dot{E}_1 = \frac{(2GM_1)^{2/3} M_1 M_2}{M_1 + M_2} (\pi f_{\rm ref})^{5/3} A_1 \left(\frac{f}{f_{\rm ref}}\right)^{2+n_1} \Theta_1, \tag{A3}$$

where

$$A_1 = \left(\frac{2\pi f_{\rm ref}}{\omega_{0,1}}\right)^{1/3} \left(\frac{\omega_{g,1}}{\Lambda_{g,1}\omega_{0,1}}\right)^2 [\beta_1 N_1 \lambda_1]_{\rm ref}$$
$$\simeq 4 \times 10^{-9} \left(\frac{\omega_{g,1}}{10^{-4}\Lambda_{g,1}\omega_{0,1}}\right)^2 [\beta_1 N_1 \lambda_1]_{\rm ref} \tag{A4}$$

is a dimensionless amplitude parameter that depends on the equation of state and how the instability saturates. The three parameters of our saturation model are therefore A_1, n_1, and $f_{0,1}$ for star 1 and similarly for star 2. We expand each of these parameters about a $1.4M_\odot$ reference mass as, e.g., $A_1 = A^{(0)} + A^{(1)}(M_1 - 1.4M_\odot) + \cdots$, where the $A^{(i)}$ are the same for both NSs. In practice, we keep only the $0^{\rm th}$ and $1^{\rm st}$ order terms in our model.

Equation (A1) then implies

$$\dot{f} = 3\pi f_{\rm ref}^2 x^{7/3} \left[B x^{4/3} + C_1 x^{n_1} + C_2 x^{n_2}\right]$$

where $x = f/f_{\rm ref}$,

$$B = \frac{32}{5} \left(\frac{G\mathcal{M}\pi f_{\rm ref}}{c^3}\right)^{5/3}, \tag{A5}$$

$$C_1 = \left(\frac{2M_1}{M_1 + M_2}\right)^{2/3} A_1 \Theta_1, \tag{A6}$$

and similarly for C_2. The phase of the GW signal $d\phi = 2\pi f dt = 2\pi f df/\dot{f}$ and

$$\phi(f) = \frac{2}{3} \int_0^{f/f_{\rm ref}} \frac{x^{-4/3} dx}{B x^{4/3} + C_1 x^{n_1} + C_2 x^{n_2}}. \tag{A7}$$

For typical NS parameters, $B \sim 10^{-4} \gg C_{1,2} \approx A_{1,2}$ if

$$[\beta N \lambda]_{\rm ref} \ll 10^5 \left(\frac{10^{-4}\Lambda_g \omega_0}{\omega_g}\right)^2. \tag{A8}$$

which we expect to be satisfied. Thus, the tidal decay due to gravitational radiation always strongly dominates and we can expand the $\phi(f)$ integrand as a power series. The phase shift relative to the PP waveform is therefore

$$\Delta\phi(f) \simeq -\frac{2}{3B^2} \int_0^{f/f_{\rm ref}} dx \left[C_1 x^{n_1 - 4} + C_2 x^{n_2 - 4}\right]$$
$$\approx \frac{1}{n-3} \left(\frac{C_{1,2}}{10^{-8}}\right) \left[\left(\frac{f_0}{f_{\rm ref}}\right)^{n-3} - \left(\frac{f}{f_{\rm ref}}\right)^{n-3}\right] {\rm rad}, \tag{A9}$$

where in the second line we assumed $n < 3$, $M_1 = M_2 = 1.4M_\odot$, and $R = 12$ km. The mass function in Eq. (7) is given by $F_1(M_1, M_2) = 2C_1/3B^2$ and similarly for F_2. The negative phase shift means that the orbit reaches a given frequency in fewer orbits than in the PP model.

Appendix B: Priors on the Model Parameters

We use a Bayesian framework to compute evidences and posterior distributions. In Table I we list the priors on all our model parameters.

Appendix C: Correlations when $n = 2$

In the main text we show the correlation between $\mathcal{M}$, q, and A only for the $n = 0$ case (see Figs. 5 and 11). However, as we show here, the trends are somewhat different when $n = 2$. Thus, the correlations can change their behavior depending on the values of the injected parameters.

The left panel of Figure 12 shows the joint and marginal distributions for $\mathcal{M}$ and q for injections with $n = 2$, $f_0 = 50\,$Hz, and $\rho_{\rm net} \simeq 50$. Unlike the monotonic increase in $\mathcal{M}$'s bias with increasing A apparent in Figure 5, here we see that $\mathcal{M}$ is biased to smaller values when A initially increases. This is because the bias in q is much stronger and pushes the posterior backward along the degeneracy between $\mathcal{M}$ and q.

The right panel of Figure 12 shows the correlation between $\mathcal{M}$ and A when $n = 2$. We see that it is reverse from the $n = 0$ case shown in Figure 11. In particular, larger A imply larger $\mathcal{M}$. This is because at smaller A, the model compensates with a more asymmetric q and a decrease in $\mathcal{M}$.

TABLE I. Prior distributions for the model parameters

	parameter	minimum	maximum	distribution
PP	M_1	$1M_\odot$	$10M_\odot$	$dN \propto dM_1$
	M_2	$1M_\odot$	$10M_\odot$	$dN \propto dM_2$
	D_L	0 Mpc	300 Mpc	$dN \propto D_L^2 dD_L$
	$\cos\theta_{jn}$	-1	1	$dN \propto d\cos\theta_{jn}$
	α	0	2π	$dN \propto d\alpha$
	$\cos\delta$	-1	1	$dN \propto d\cos\delta$
NL	$A(1.4M_\odot)$	10^{-10}	10^{-5}	$dN \propto d\log A$
	$\frac{1}{A}dA/dm(1.4M_\odot)$	$-1M_\odot^{-1}$	$1M_\odot^{-1}$	$dN \propto d(\log A/dm)$
	$f_0(1.4M_\odot)$	10 Hz	100 Hz	$dN \propto df_0$
	$df_0/dm(1.4M_\odot)$	$-10\,\mathrm{Hz}/M_\odot$	$10\,\mathrm{Hz}/M_\odot$	$dN \propto d(df_0/dm)$
	$n(1.4M_\odot)$	-1	3	$dN \propto dn$
	$dn/dm(1.4M_\odot)$	$-1M_\odot^{-1}$	$1M_\odot^{-1}$	$dN \propto d(dn/dm)$

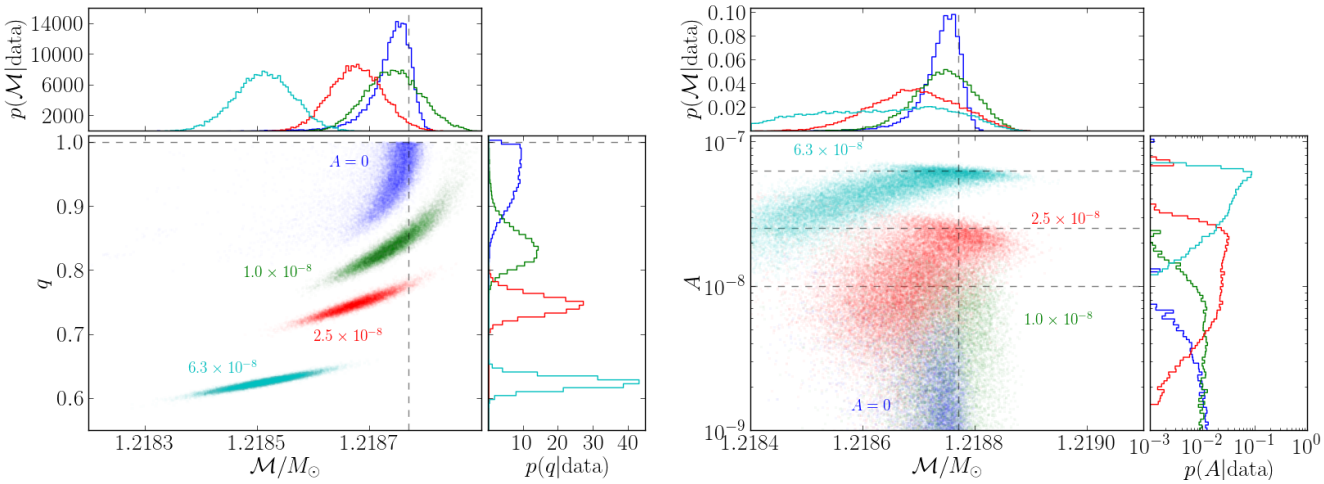

FIG. 12. Joint and marginal posterior distributions of $\mathcal{M}$, q, and A for various values of A. We take $f_0 = 50\,\mathrm{Hz}$ and $n = 2$, and inject the signals at $\rho_{\mathrm{net}} \simeq 50$.